Analysis of 205-nm photolytic production of atomic hydrogen in methane flames

W.D. Kulatilaka · J.H. Frank · B.D. Patterson · T.B. Settersten

Abstract We investigate the 205-nm photolytic production of atomic hydrogen in methane flames. This process represents a significant interference in two-photon, laser induced-fluorescence (TP-LIF) detection of atomic hydrogen in flames. Relative TP-LIF profiles of the photolytically produced H atoms were measured using a pump-probe technique in atmospheric-pressure, premixed $CH_4/O_2/N_2$ flames. A high-fluence, non-resonant, nanosecond pump laser created H atoms by photodissociating flame constituents, and a copropagating, non-perturbing picosecond laser probed the photolytically produced H atoms via TP-LIF. Spatial profiles of photolytically produced H atoms indicate that both intermediate and product species contribute to the interference in all flames. Excellent agreement between simulated and measured interference signals is observed in the product region of the flames. Vibrationally excited H_2O is the dominant source of interference in the product region, but an additional contribution is attributed to vibrationally excited OH radicals. In the flame-front region, CH_3 is the dominant precursor, and photodissociation of C_2H_2 becomes increasingly important in rich flames. Mechanisms for sequential photodissociation of CH_3 and C_2H_2 are presented, indicating that complete dissociation at 205 nm of both precursors is feasible.

PACS 42.62.Fi · 33.50.-j · 33.80.Gj · 82.33.Vx

W.D. Kulatilaka · J.H. Frank · B.D. Patterson ·
T.B. Settersten (✉)
Combustion Research Facility, Sandia National Laboratories,
Livermore, CA 94551, USA
e-mail: tbsette@sandia.gov
Fax: +1-925-2942595

1 Introduction

Multiphoton laser-induced fluorescence (LIF) has been used for detection of atomic hydrogen (H) in flames for over two decades [1–10]. A particularly attractive feature of LIF is its excellent spatial resolution, which can be extended to a two-dimensional planar configuration by using a laser sheet for excitation and an intensified camera for detection [11, 12]. The simplest and most widely used approach employs two 205-nm photons for excitation from the ground $1s\,^2S$ state to the second excited level ($3s\,^2S$, $3d\,^2D$) [1–4]. The resulting fluorescence from the H_α transition ($n = 3 \rightarrow n = 2$) is detected at 656 nm.

Although the two-photon-resonant LIF technique (TP-LIF) using 205-nm excitation is straightforward in principle, its reliable application in flame research has been hindered by the unintended generation of atomic hydrogen by ultraviolet (UV) photodissociation of certain flame species. The photolytically produced H atoms interfere with the measurement of the nascent H atoms in the flame because they are two-photon excited by the same laser pulse and contribute to the total TP-LIF signal. Early in the development of this approach for combustion research applications, Goldsmith [13] demonstrated that the intense 205-nm laser pulses used to excite H-atom fluorescence simultaneously photodissociated vibrationally excited water vapor in H_2/O_2 flames. Subsequently, Desgroux et al. [14, 15] demonstrated that photodissociation of methyl radicals (CH_3) was responsible for the creation of hydrogen atoms in the reaction zone of low-pressure methane/air flames. Furthermore, a number of other flame species such as hydroxyl (OH) [16], acetylene (C_2H_2) [17], methylene (CH_2) [18], formyl (HCO), carboxyl (–COOH), vinyl (C_2H_3), and allyl (C_3H_5) radicals [19] are known to produce hydrogen atoms via 205-nm photodissociation.

In previous work [20], we demonstrated that the impact of the photolytically produced H atoms can be reduced in some cases by decreasing the duration of the excitation pulse from the nanosecond (ns) to the picosecond (ps) regime. A similar finding was observed in an analogous investigation of TP-LIF detection of atomic oxygen, for which photodissociation of vibrationally excited CO_2 and O_2 causes measurement interference [21]. The improvement afforded by short-pulse excitation is rationalized as follows. Single-photon photodissociation of photolytic precursors results in a concentration of photolytically produced atoms (i.e., the relative interference) that increases linearly with pulse energy. Because the TP-LIF signal scales quadratically with pulse irradiance, by reducing the pulse duration, a lower-energy excitation pulse can be used to produce a particular TP-LIF signal level, thus reducing the relative measurement interference.

In [20], one-dimensional (1-D) radial line images of H-atom fluorescence were produced in a series of premixed CH_4 and H_2 Bunsen flames. A range of laser fluences was used to determine at which point photolytic interference affected the measurement. At the lowest fluences, the contribution to the TP-LIF signal from photolytically produced H atoms was not detectable, and the shape of the fluorescence profiles was independent of laser fluence. For these conditions, the measurements were considered "interference-free." At higher fluences, however, the photolytic contribution increased to the point that it produced a measurable distortion in the shape of the profile. By comparing the peak-normalized profiles for an appropriate range of fluence, the maximum interference-free signal and the associated fluence were determined in each flame. This approach is most sensitive when the spatial distributions of the photolytic precursors and the nascent H atoms in the flame are significantly different. For example, the interference in the flame products (presumably from photodissociation of water vapor) was clearly discernible in [20] because the interference peak was well separated from the peak H-atom TP-LIF signal. On the other hand, the interference from intermediate species, which occurred in a narrow region close to the location of the H-atom peak, was much more difficult to infer from changes in the TP-LIF profile.

In the present work, we remove this ambiguity in the identification of the photolytic contributions to the measured TP-LIF signal by using a pump-probe technique. The pump-probe technique enables straightforward determination of the spatial distribution of the photolytic interference and provides a direct calibration of the number density of the photolytically produced H atoms relative to those occurring naturally in the flame. Using 1-D laminar flame models, we evaluate the significance of photodissociation of H_2O, CH_3, and other H-containing species that are present in relatively high concentration in the series of premixed CH_4

flames investigated in [20]. The results implicate photodissociation of vibrationally excited H_2O and OH in the product region and photodissociation of CH_3 and C_2H_2 near the flame front.

The experimental apparatus and procedure are described in the following two sections; flame calculations and modeling of the photolytic interference are described in Sect. 4; results of pump-probe measurements in a series of $CH_4/O_2/N_2$ flames are presented in Sect. 5; and a discussion of the results follows in Sect. 6.

2 Experimental apparatus

The experimental apparatus consisted of an axisymmetric premixed flame, a tunable ns-laser system, a tunable ps-laser system, and an intensified charge coupled device (ICCD) camera. The setup is identical to the one used previously for single-laser line imaging of atomic hydrogen using either ns or ps pulses to excite the fluorescence [20]. In the current two-laser experiments, the ns laser photodissociated H-containing precursors in premixed CH_4 flames, and the ps laser probed the photolytically produced H atoms and the nascent H atoms in the flame. A brief description of the apparatus follows.

We investigated six atmospheric-pressure, laminar, premixed $CH_4/O_2/N_2$ Bunsen flames with equivalence ratios in the range of $0.51 \leq \Phi \leq 1.64$. The flames were stabilized on a 6-mm-diameter nozzle, and the gas flows were set so that the height of the inner cone of all flames was approximately 11 mm above the burner nozzle. The flow conditions were identical to those specified in [20].

The "pump" pulses were generated by frequency tripling the output of a commercial dye laser system that was pumped by the second-harmonic of an injection-seeded Nd:YAG laser operating at a 20-Hz repetition rate. The UV pulse duration was approximately 3.5 ns, and the maximum pulse energy available at the probe volume was 1.5 mJ. Based on the line width of the fundamental, we estimate a UV line width of approximately 0.5 cm^{-1}. Although the laser was tunable, for most experiments the pump laser wavelength was set to 204.811 nm, which is 0.333 nm from the H-atom two-photon resonance at 205.144 nm.

The "probe" pulses were generated using a custom-built, frequency-tripled, distributed-feedback dye laser system (DFDL) that operated at 20 Hz [22]. The estimated UV pulse width was 70 ps, and the line width was less than 1 cm^{-1}. The DFDL was tuned to excite the H-atom two-photon transitions at 205.144 nm ($3s\,^2S$, $3d\,^2D \leftarrow\leftarrow 1s\,^2S$). The probe pulse energy was limited to ≤ 10 μJ, in accord with the interference-free limits that were identified in [20] for the current flames. The probe pulse was delayed by several ns with respect to the pump pulse, and the timing jitter was better than ± 2 ns.

The pump and probe beams were weakly focused using 1-m focal-length UV lenses and horizontally crossed at an angle of approximately 0.5° and a height of 3.75 mm above the burner nozzle. The diameters of the pump and probe beams were approximately 250 and 200 μm, respectively, throughout the sample volume, and the spatial profiles were nearly top hat. The overlap of the beams was optimized by maximizing the fluorescence signal when both pump and probe beams were present.

To ensure that stimulated emission (SE) did not perturb the fluorescence measurements, we checked for forward-propagating SE using the detection scheme described in [20]. Although the probe laser fluence was well below the SE thresholds reported in [20], the increased H-atom densities from photodissociation by the pump pulse could, in principle, result in lower thresholds in the current experiments. Indeed, in the $\phi = 1.64$ flame, we observed a very weak SE signal at the highest available pump fluence of $3.05 \, \mathrm{J\,cm^{-2}}$. Stimulated emission was not observed, however, for lower pump fluence in the $\phi = 1.64$ flame and for all fluences in the other flames. Therefore, we assert that the fluorescence signals were not perturbed by SE.

The 656-nm fluorescence generated by the probe pulse was collected and imaged onto an ICCD camera using two camera lenses. An H_α filter with a 3-nm bandpass was placed between the two lenses to pass the H-atom TP-LIF and to block out-of-band interference. The first half of the flame that was intersected by the laser beams was imaged, and a single pixel in the image corresponded to 25 μm in the flame. The intensifier gate was centered around the pump and probe pulses, and the gate width was set to 400 ns.

3 Experimental procedure

A series of pump-probe measurements was conducted for a range of pump pulse fluences in each flame. Three sets of fluorescence line images were acquired at each pump fluence: those with only the probe laser present, those with only the pump laser present, and those with both pump and probe lasers present. For each image set, on-chip averaging (80–200 laser shots) was used, and between 10 and 20 frames were averaged to improve signal-to-noise ratios. All images were corrected for background by subtracting an image taken with all laser beams blocked. For the current experimental conditions, flame luminosity was negligible, and the background images were essentially dark images. The background-corrected images were integrated in the vertical direction over the width of the laser beam to obtain radial profiles of the corresponding signals.

Figure 1 shows an example of the pump-only ("pu"), probe-only ("pr"), and pump-probe ("pu-pr") profiles for the $\phi = 0.97$ flame at a pump fluence of $1.90 \, \mathrm{J\,cm^{-2}}$, where
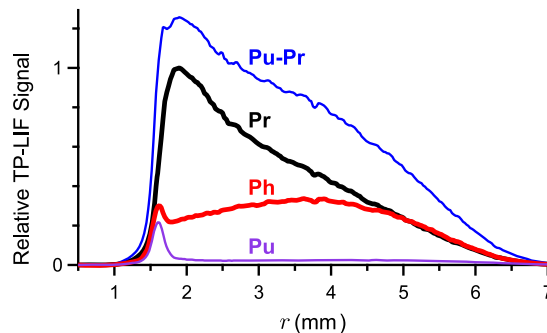

Fig. 1 Radial profiles measured with the pump-only (pu), probe-only (pr), and pump and probe lasers together (pu-pr). The profile of the photolytically produced H atoms is labeled "ph." The measurements were conducted in the $\Phi = 0.97$ flame using a pump fluence of $1.9 \, \mathrm{J\,cm^{-2}}$

all profiles are scaled relative to the peak signal of the probe-only profile. In Fig. 1, the burner axis corresponds to $r = 0$, and the reactants span the region approximately between $0 \leq r < 1.5$ mm. The flame front is located near $r = 1.5$ mm, and reactive intermediates are located roughly between 1.5 and 1.8 mm. The flame products extend to larger radial distances. The lasers propagated from right to left in the figure.

The probe-only signal is the interference-free TP-LIF signal that was generated by the nascent atomic hydrogen in the flame. The pump-only signal contains no contribution from atomic hydrogen fluorescence, but instead results from pump-induced-fluorescence interference from other flame species. Based on spectrally and spatially resolved emission measurements using an imaging spectrograph, we expect that this signal resulted from photofragment emission from hydrocarbon intermediates that leaked through the H_α filter onto the ICCD; we observed strong pump-induced CH and C_2 emissions in the 400–600 nm range that were localized in the flame front. Similar observations were reported by Georgiev and Aldén [11] and Gasnot et al. [15]. The pump-probe signal contains contributions from both the pump-only and probe-only profiles as well as from the TP-LIF signal that is generated from the H atoms that are photolytically produced by the intense pump pulse.

Profiles of the photolytic interference were determined by subtracting from each pump-probe fluorescence profile the associated profiles that were produced when the pump and probe lasers were independently pulsed. The curve labeled "ph" in Fig. 1 is the photolytic-interference profile that was generated by a pump fluence of $1.90 \, \mathrm{J\,cm^{-2}}$ in the $\Phi = 0.97$ flame. The same procedure was used to measure photolytic-interference profiles for a range of fluences in all six flames.

4 Modeling

4.1 One-dimensional flame calculations

One-dimensional laminar flame calculations using the Sandia PREMIX code [23] with GRI-Mech 3.0 [24] or Miller's Mechanism [25, and references therein] estimated the flame composition and temperature as a function of position normal to the flame front in the six $CH_4/O_2/N_2$ flames. For the Miller Mechanism, nitrogen chemistry was neglected, and species containing greater than three carbon atoms were omitted. Although the 1-D calculations do not include the effects of flame curvature or heat loss, these effects are least significant on the sides of the flames where the measurements were performed. We do, however, restrict comparisons between measured and calculated spatial profiles to radial locations $r < 4$ mm because the calculations do not account for the significant mixing of the flame products with the cold surrounding air. At the measurement location, the flame normal was sufficiently close to horizontal that the radial coordinate probed by the lasers closely approximated the flame-normal coordinate in the calculations. The measured and calculated spatial profiles were matched by aligning the locations of the peak H-atom TP-LIF signal and the peak H-atom concentration from the calculations.

Results of the GRI-Mech calculations are shown in Figs. 2 and 3 for the six flames. In Fig. 2, the calculated

temperature and number densities of H, H_2O, H_2, and OH are shown with the unburned reactant region at $r = 1$ mm and the hot combustion products at $r = 4$ mm. In Fig. 3, relative number densities of transient intermediate species are shown, and the radial coordinate is scaled to focus on the thin reaction zone. In all flames investigated here, CH_3 is the most abundant intermediate species, although the other intermediates shown in Fig. 3 will also be discussed subsequently.

The accurate prediction of intermediate species in flames remains a challenge, and results can vary significantly for different chemical mechanisms. As a result, it is important to consider more than one mechanism when comparing measured interferences with computed profiles of intermediate species. We compare results from PREMIX calculations using GRI-Mech 3.0 and Miller's Mechanism. In all six flames, the predicted flame temperatures and H_2O number densities are identical for both mechanisms. The predictions of the OH number densities are also comparable for both mechanisms with the largest discrepancy of 17% occurring in the product region of the $\Phi = 0.51$ flame. The ratio of peak H_2 number densities for the Miller and GRI Mechanisms increases monotonically with equivalence ratio and ranges from 0.7 in the $\Phi = 0.51$ flame to 1.1 in the $\Phi = 1.64$ flame. For Miller's Mechanism, the peak H-atom number densities are 20–30% lower than for GRI-Mech in

Fig. 2 Results of 1-D laminar flame calculations with GRI-Mech 3.0 for temperature (*dotted curve*) and number densities of H (*thick solid curve*), H_2O (*thin solid curve*), H_2 (*dashed curve*), and OH (*dash-dot curve*) in each of the six $CH_4/O_2/N_2$ flames with equivalence ratios: (**a**) 0.51, (**b**) 0.70, (**c**) 0.97, (**d**) 1.14, (**e**) 1.39, and (**f**) 1.64. Note that curves for H_2O and H_2 have been scaled by 0.1 to plot all number densities on the same vertical scale
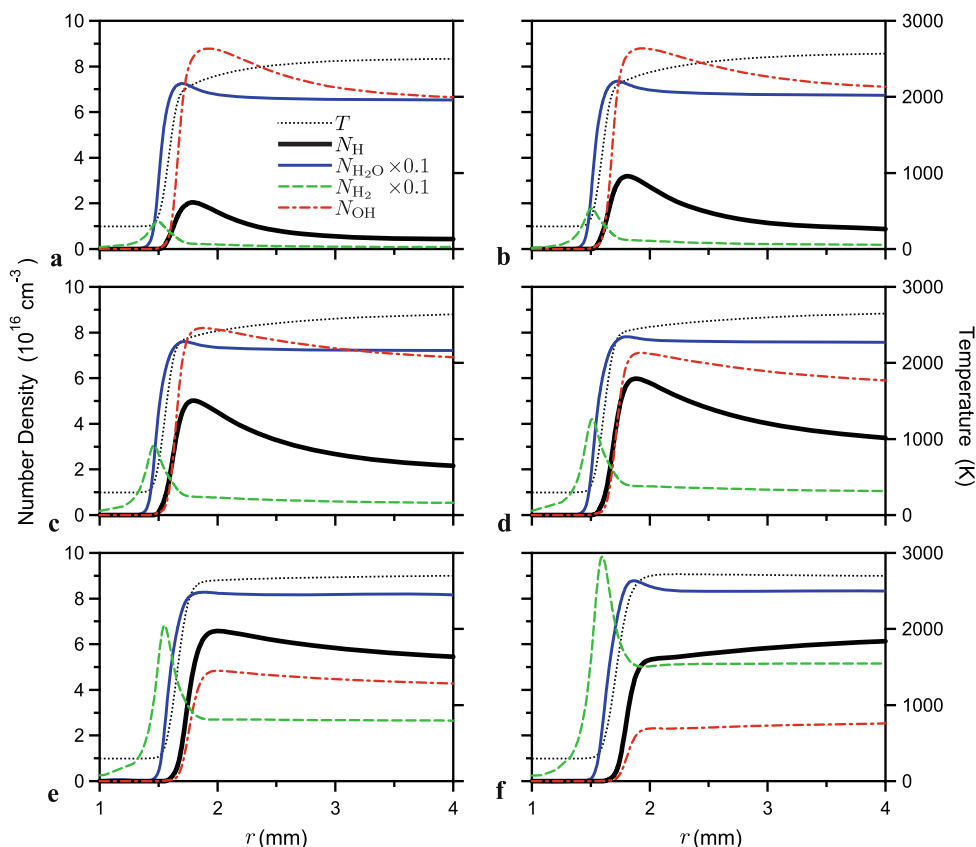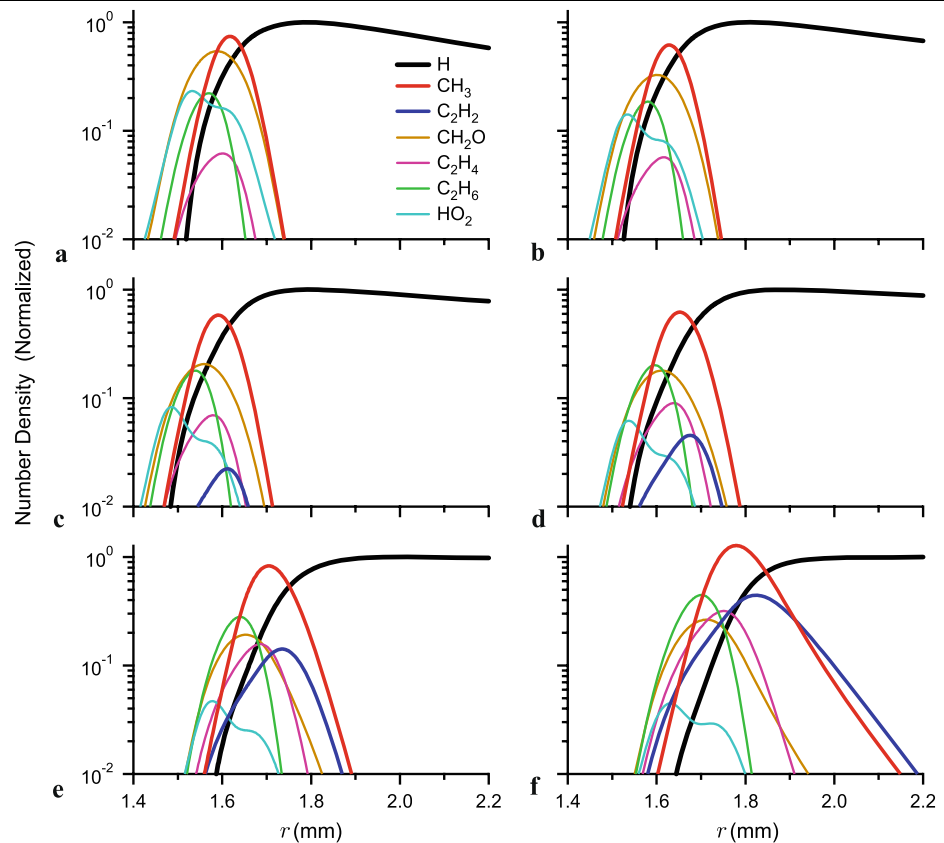
Fig. 3 Results of 1-D laminar flame calculations with GRI-Mech 3.0 for number densities of combustion intermediate species in each of the six $CH_4/O_2/N_2$ flames with equivalence ratios: (**a**) 0.51, (**b**) 0.70, (**c**) 0.97, (**d**) 1.14, (**e**) 1.39, and (**f**) 1.64. Number densities in each flame have been normalized to the maximum number density of atomic hydrogen in the plotted region


the flame-front region. The two richest flames, $\Phi = 1.39$ and 1.64, have distinctly different profiles for the two mechanisms. In the $\Phi = 1.39$ flame, the Miller Mechanism shows a gradual increase of the H-atom number density in the product region, whereas GRI-Mech peaks in the reaction zone and decays in the product region. In the $\Phi = 1.64$ flame, the Miller Mechanism predicts a lower H-atom number density in the reaction zone with a steeper rise in number density in the products region.

The differences between GRI-Mech and Miller's Mechanism that are most significant for the present study pertain to intermediate hydrocarbon species. Figure 4 compares the predicted number densities of CH_3 and C_2H_2, which are important precursor molecules for photolytic production of atomic hydrogen, as will be discussed in Sect. 6.2. The number density profiles are normalized by the corresponding peak H-atom number density near the flame front for each mechanism because the significance of H-atom LIF interferences from photodissociation depends on the relative number densities of atomic hydrogen and precursor molecules. For the two lean flames, Miller's Mechanism predicts an order of magnitude larger number densities of C_2H_2 than GRI-Mech. However, the peak C_2H_2 number densities are less than 10% of the peak H-atom number densities, and therefore C_2H_2 is of secondary importance as a photolytic

precursor in the lean flames. In contrast, Miller's Mechanism predicts peak C_2H_2 number densities in the $\Phi = 1.39$ and 1.64 flames that are respectively 50% and 110% of the H-atom number densities at the flame front. In these two rich flames, the Miller Mechanism predicts that the ratio of C_2H_2 to H-atom number densities at the flame front are approximately 2–4 times larger than for the GRI-Mech calculation. This result indicates that contributions from C_2H_2 to photolytic interference is potentially quite significant in the rich flames and may be underestimated by GRI-Mech.

In all six flames, the methyl radical has the highest number density of the intermediate hydrocarbon species and may be a significant precursor for photolytic production of atomic hydrogen at the flame front. The Miller Mechanism consistently predicts higher peak number densities of CH_3 than GRI-Mech, although the discrepancy decreases as the equivalence ratio increases. In the $\Phi = 0.51$ and 1.64 flames, the peak CH_3 number densities for the Miller Mechanism calculation are approximately 60% and 7% greater than for the GRI-Mech calculation, respectively. For all six flames, both mechanisms indicate that the peak CH_3 number densities exceed 50% of peak H-atom number densities at the flame front. In several flames, the calculations show CH_3 number densities that are comparable to or greater than the H-atom number densities.

Fig. 4 Comparison of results of 1-D laminar flame calculations using GRI-Mech 3.0 (*solid curves*) and the Miller Mechanism (*dashed curves*) for number densities of H, CH_3, and C_2H_2 in each of the six $CH_4/O_2/N_2$ flames with equivalence ratios: (**a**) 0.51, (**b**) 0.70, (**c**) 0.97, (**d**) 1.14, (**e**) 1.39, and (**f**) 1.64. Number densities in each flame have been normalized to the maximum number density of atomic hydrogen in the plotted region
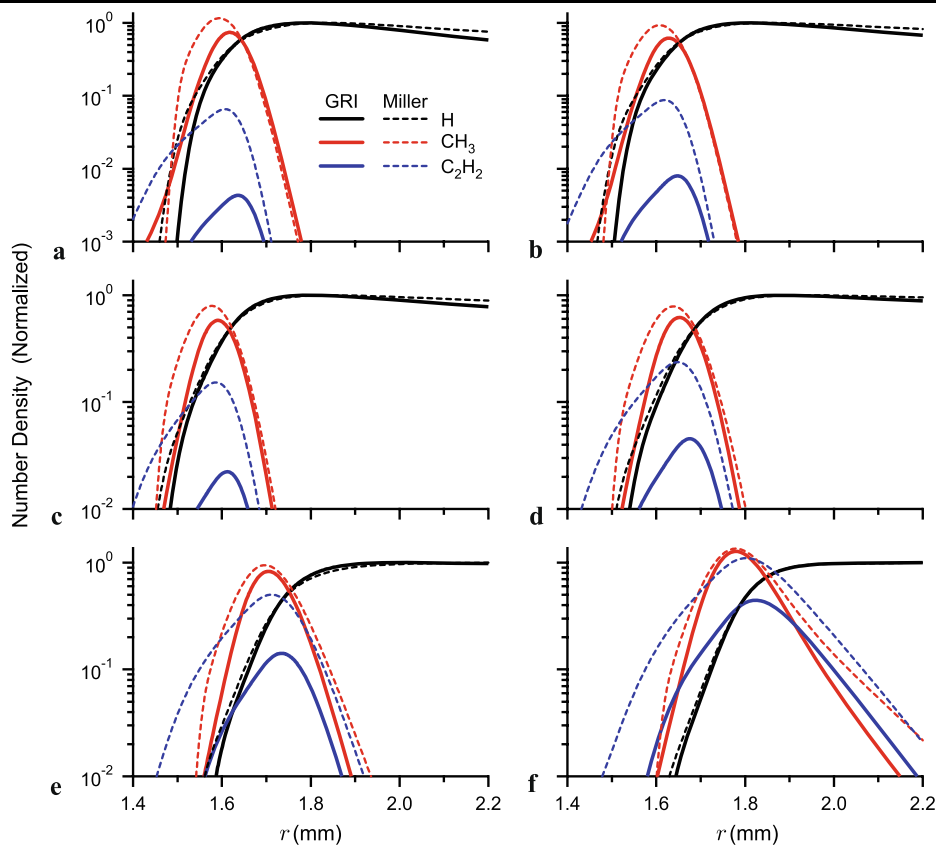
4.2 LIF model

Results of the 1-D flame calculations were used in a LIF model to simulate the experimentally measured LIF profiles. In the absence of interference, the measured LIF signal is directly proportional to the product of the H-atom number density and the fluorescence quantum yield, which is inversely proportional to the fluorescence quenching rate. Based on limiting models for the temperature-dependent quenching cross sections, as described in [20], and the calculated temperature and composition of the flames, we estimate that variations in the quenching rate are minor for locations between the H-atom TP-LIF peak and the products in each flame. The quenching rate does change significantly for radial locations where the flame products mix with the surrounding air, however, and analyses are limited to $r < 4$ mm to avoid this complication, as indicated in the previous section. Consequently, corrections for quenching rate variations are omitted, and the fluorescence signal, S_{LIF}, in each flame is modeled as the spatial convolution of the calculated number density of atomic hydrogen, $N_H(r)$, and the instrument response function, $g(r)$, for the detection system,

$$S_{LIF}(r) = C N_H(r) \otimes g(r), \tag{1}$$

where the "$\otimes$" symbol indicates a spatial convolution, and C is a normalization constant.

The instrument response function, or line-spread function, was determined from the derivative of the step-response function, which was measured by imaging a knife edge. The measured response function was fitted using a sum of Lorentzian and Gaussian functions. A Lorentzian function with a full-width at half-maximum (FWHM) of 72 µm accounted for the main response. Small residuals in a single Lorentzian fit appeared in the wings of the response and were fitted with Gaussian functions that were peaked at ±285 µm with respect to the Lorentzian peak and had a FWHM of 270 µm. The Gaussian amplitude was 2% of the Lorentzian amplitude.

Equation (1) was used to simulate the measured probe-only profiles resulting from the nascent H atoms in each flame. Excellent agreement between the measured and calculated profiles is shown in Fig. 5. The same function $g(r)$ was used in all cases, but the normalization constant in (1) was determined for each flame.

The same convolution and normalization constants were used to predict fluorescence signals from photolytically generated H-atoms. In this case, the H-atom number density in (1) was replaced with the number density of the photolytically produced H atoms, N_H^{ph} [cm^{-3}]. We express N_H^{ph} as a sum of contributions from relevant photolytic precursors at
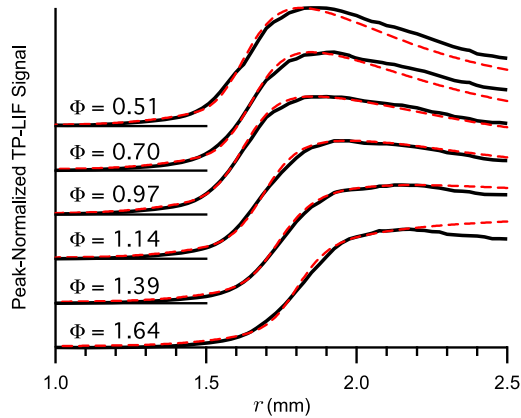
Fig. 5 Peak-normalized probe-only LIF profiles (*solid curves*) and simulated LIF profiles (*dashed curves*) in each of the six CH$_4$/O$_2$/N$_2$ flames. Profiles are vertically offset for display

a particular location, r,

$$N_H^{ph}(r) = \sum_i N_i^{eq}(r)\eta_i \left(1 - \exp\left[-\frac{F}{h\nu}\sigma_i(T)\right]\right), \qquad (2)$$

where N_i^{eq} is the nascent number density of the ith precursor molecule [cm^{-3}], σ_i is the temperature-dependent absorption cross section of the ith precursor [cm^2], F is the laser fluence [J cm^{-2}], and $h\nu$ is the photon energy [J]. The variable η_i is the yield of H-atoms that result from photodissociation of the ith precursor and that are detected by the probe beam ($0 \le \eta_i \le 1$). It is important to note that η_i may be less than the true H-atom photodissociation yield if the photodissociation process produces translationally hot atoms that are not detected because they either fly out of the probed volume or are not in-resonance with the probe laser because of the Doppler shift associated with the component of the product velocity along the probe laser propagation direction.

Equation (2) describes the photolytic production of atomic hydrogen resulting from single-photon photodissociation. Although it is possible that multi-photon-resonant absorption can lead to production of H atoms, we assume these processes are much weaker than single-photon-resonant absorption at 205 nm.

Equation (2) accounts for depletion of the precursor molecules and assumes that collisional redistribution is sufficiently rapid that the precursor population distribution remains thermalized during the laser pulse. As the ground-state population becomes depleted, the photolysis process saturates. Saturation is important when the product of the absorption cross section and photon fluence becomes large. At the highest fluences used in the current experiments, slight saturation is predicted for absorption cross sections that are on the order of 10^{-19} cm^2. For strong absorbers ($\sigma \ge 10^{-18}$ cm^2), significant saturation is expected at the highest fluences.

5 Results

Figure 6 presents the results of pump-probe measurements in the six CH$_4$/O$_2$/N$_2$ flames. The thick curves are the interference-free TP-LIF (probe-only) profiles resulting from the nascent H atoms in each flame. The thin curves are the photolytic-interference profiles in each flame for a series of pump laser fluences. All profiles are scaled relative to the nascent H-atom TP-LIF peak in each flame, which is located at approximately $r = 2$ mm. The minimum pump fluence used in all flames was approximately 0.6 J cm^{-2}, which is 4–10 times larger than the interference-free limits reported in [20]. Therefore, the magnitudes of the interference are a significant fraction of the interference-free signals in these flames.

The reported pump-probe measurements were conducted with the probe laser delayed several ns with respect to the pump laser. We observed no measurable change in the photolytic signal for pump-probe delays up to 100 ns. The observation that the measured yield η_i did not change on this time scale demonstrates that the measurements were not sensitive to thermalization of translationally hot H-atoms produced in the photodissociation process. This observation does not, however, exclude the possibility that some fast H atoms flew out of the volume defined by the spatial overlap of the pump and probe beams without being detected. For longer delays, a single-exponential decay with a 5-μs time constant was measured. This time constant is consistent with diffusion of (thermalized) photolytically produced H atoms out of the probe volume.

Although the interference profiles were measured with the pump laser tuned to 204.811 nm, we expect that these measurements are representative of the interferences that are produced when the laser is tuned to the two-photon H-atom resonance at 205.144 nm. This expectation is based on the assumption that the precursor absorption spectrum is broad and featureless because of short-lived predissociative or repulsive excited states. This assumption is consistent with the absorption spectra of the previously implicated photolytic precursors of H atoms in flames. When scanning the photolysis laser from 204.6 to 205.9 nm, Goldsmith [13] saw no significant change in the production of OH fragments in the photodissociation of water vapor (H$_2$O + $h\nu \rightarrow$ H + OH) in an atmospheric-pressure H$_2$/O$_2$ flame. Similarly, Desgroux and coworkers [14] observed no change in the efficiency of photofragment emission from CH$_3$ radicals in flames over the range 202.6–208.3 nm. Because it is possible that some other, yet unidentified, precursors contributed to the interference, it was necessary to ensure that there was no significant dependence of the interference signal on the pump wavelength in the current experiment. As a check, we tuned the pump laser between 204.078 and 204.811 nm, and observed no measurable change in the interference.

Fig. 6 Photolytic-interference profiles for a range of pump fluence in each of the six $CH_4/O_2/N_2$ flames with equivalence ratios: (**a**) 0.51, (**b**) 0.70, (**c**) 0.97, (**d**) 1.14, (**e**) 1.39, and (**f**) 1.64. Pump fluence [$J\,cm^{-2}$] is indicated in the legend, and the interference-free TP-LIF profiles of nascent H atoms in each flame are shown as the *thick solid curves*. Interference profiles are scaled relative to the nascent profile in each flame
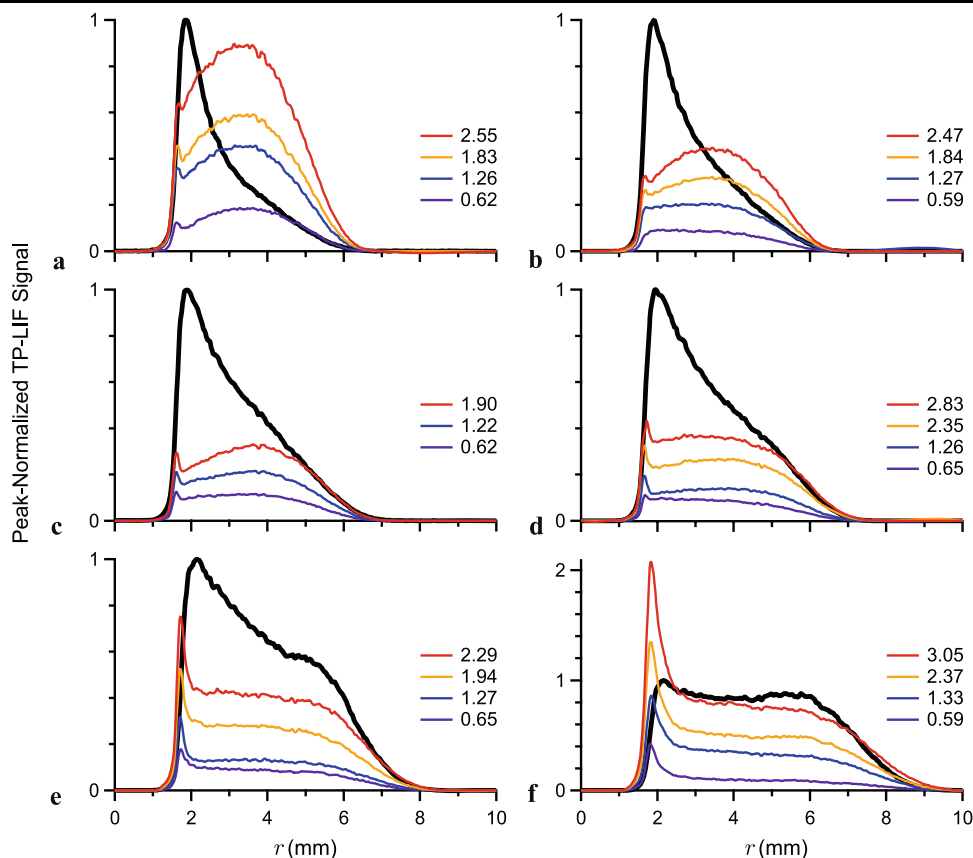
6 Discussion

The broad spatial distribution of the photolytic-interference profiles in Fig. 6 is consistent with the photodissociation of product species. In the region near the flame front (1.5 mm $< r <$ 2 mm), the photolytic-interference profiles display a sharp peak, which is consistent with photodissociation of reactive intermediate species. This feature is clearly visible for all of the flames, including the leanest flame (Fig. 6a). Interferences in the flame front of the lean flames were previously undetectable with single-laser measurements in [20].

The relative shape of the interference profile depends on the equivalence ratio. In the $\phi = 0.51$ flame (Fig. 6a), the peak photolytic interference at the highest pump fluence (2.55 $J\,cm^{-2}$) occurs in the flame products and nearly equals the peak signal from nascent H atoms. The magnitude of the interference in the vicinity of the flame front is relatively small compared to the interference in the products. In the $\Phi = 0.97$ flame, with a pump fluence of 1.90 $J\,cm^{-2}$ (Fig. 6c), the photolytically produced signals near the flame front and in the products are nearly equal in magnitude and correspond to approximately one-third of the peak interference-free signal. In the rich flames (Figs. 6d–f), the photolytic interference near the flame front becomes more significant in comparison to the interference in the flame

products. In the $\Phi = 1.64$ flame (Fig. 6f), the interference near the flame front is 2–3 times larger than that in the products, and at the highest fluence (3.05 $J\,cm^{-2}$), it is more than 2 times larger than the peak interference-free TP-LIF signal.

These data clearly indicate that all of the flames were affected by photolytic precursors that exist in the flame products and in the vicinity of the flame front. The relative importance of the interference resulting from photodissociation of these two types of precursors depends on the equivalence ratio. In the following two sections, interference from the precursor types are discussed with the aid of the 1-D flame calculations and the model for the photolytic interference, (2).

6.1 Interference in the product region

In the product region of the six CH_4 flames, there are three H-containing species that are present in concentrations comparable to or greater than that of the nascent H-atoms: molecular hydrogen (H_2), hydroxyl radical (OH), and water vapor. The distributions of these species from the laminar flame calculations using GRI-Mech are shown in Fig. 2. Water vapor is the most abundant of the suspected precursors, with a number density of almost 10^{18} cm^{-3}. In the product region of the $\Phi = 0.51$ flame, the number density of H_2O is almost two orders of magnitude greater than that of atomic hydrogen. This ratio decreases with increasing equivalence

ratio, but remains larger than 10 in all flames. The spatial distribution of OH molecules extends well into the product region. The ratio of OH to H-atom concentration decreases with increasing equivalence ratio, with a maximum value of $N_{OH}/N_H \approx 10$ in the $\Phi = 0.51$ flame. The opposite trend characterizes the H_2 concentration in the product region of the flames. At $r = 2.6$ mm, the calculated number density of H_2 is comparable to that of H atoms in the lean and stoichiometric flames, and their ratio increases with increasing equivalence ratio. In the $\Phi = 1.14$, 1.39, and 1.64 flames, the H_2 number density exceeds the peak H-atom number density by factors of 2, 4, and 8, respectively.
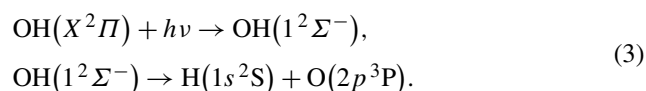
We consider the potential interference posed by photodissociation of H_2, OH, and H_2O. The relevant processes for these species and modeling of the resulting interference are presented below.

6.1.1 Molecular hydrogen (H_2)

Despite its relative abundance in the flames, we can eliminate H_2 from the list of potential precursors. Although single-photon photodissociation of molecular hydrogen occurs in the vacuum UV, two-photon excitation near 205 nm to the EF state can lead to subsequent photodissociation. The two-photon transitions are sharp, however, and an examination of line positions for transitions from all significantly populated levels indicates no coincidental overlap with either the two-photon H-atom resonance at 205.144 nm or the pump laser wavelength at 204.811 nm [26, 27]. The closest transitions are the $O(10)$ transition in the (1,0) band and the $S(0)$ transition in the (1,1) band, which are both 50 cm^{-1} from the two-photon frequency of the H-atom resonance. Furthermore, at 2500 K the lower-state population fractions for these weak transitions are only 0.02 and 0.003, respectively.

6.1.2 Hydroxyl radical (OH)

Vibrationally excited OH $X^2\Pi(v)$ molecules can be photodissociated with a single photon at 205 nm. Excitation to the repulsive potential of the $1\,^2\Sigma^-$ state produces ground-state hydrogen and oxygen atoms,

$$\begin{aligned} OH(X^2\Pi) + h\nu &\rightarrow OH(1\,^2\Sigma^-), \\ OH(1\,^2\Sigma^-) &\rightarrow H(1s\,^2S) + O(2p\,^3P). \end{aligned} \quad (3)$$
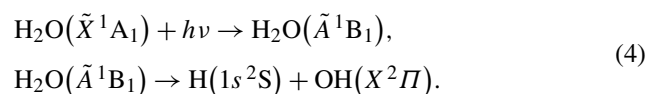
Recent experiments and calculations of the vibrational-level-dependent photodissociation for OH indicate that the photodissociation cross sections are approximately 1×10^{-22}, 4×10^{-20}, and 5×10^{-19} cm^2 for $v = 0$, 1, and 2, respectively [16]. The interference from OH photodissociation is limited because the ground vibrational state of OH, which accounts for more than 85% of the population distribution at

temperatures relevant to the current experiment, contributes negligibly to this process. Based on the cross sections from [16], we estimate that no more than 3% of the nascent OH is photodissociated at the highest pump fluences used in the current experiments. Using (1) and (2) to simulate the interference signal, the contribution from photodissociation of OH accounts for less than 10% of the measured interference in the $\Phi = 0.51$, 0.70, 0.97, and 1.14 flames. In the $\Phi = 1.39$ and 1.64 flames, the calculated interference is less than 6% and 3%, respectively, of the measured interference.

6.1.3 Water vapor (H_2O)

Water vapor is the most abundant suspect, and 205-nm photodissociation of vibrationally excited H_2O has been shown previously to produce H atoms in flames. Excitation to the first excited state leads to direct dissociation [28],

$$\begin{aligned} H_2O(\tilde{X}\,^1A_1) + h\nu &\rightarrow H_2O(\tilde{A}\,^1B_1), \\ H_2O(\tilde{A}\,^1B_1) &\rightarrow H(1s\,^2S) + OH(X^2\Pi). \end{aligned} \quad (4)$$

Equation (2) was used to simulate the number density of H atoms resulting from photodissociation of water vapor in the flames. We used the temperature-dependent absorption cross section for H_2O from [29] and the temperature and number density of H_2O from the 1-D flame calculations shown in Fig. 2. The yield, η_{H_2O}, was used as a fitting parameter. The calculated number density of H-atoms produced from H_2O photodissociation was added to that from OH photodissociation and convolved with the spatial response function, $g(r)$, according to (1) to simulate the photolytically generated fluorescence signal. By adjusting only η_{H_2O} as a scaling parameter, excellent agreement between simulated and measured interference profiles was possible. An example of a fit to the data for the $\Phi = 0.97$ flame is shown in Fig. 7a. In this case, all three measured interference profiles are fit using a value of $\eta_{H_2O} = 0.1$. The agreement is excellent, in terms of both the magnitude and the shape of the profiles. The model and measured profiles depart, however, for $r > 4$ mm. We assume that this disagreement is the result of the product gases mixing with the surrounding air, an effect that is not included in the 1-D flame calculations.

Generally, the interference profiles in a particular flame were not universally fitted with a single value of η_{H_2O} as in Fig. 7a. For example, Fig. 7b presents results of the model–experiment comparison for the $\Phi = 0.51$ flame. In this case, using a fixed value of $\eta_{H_2O} = 0.1$ caused the calculated profiles to over-predict the lowest energy profile and to under-predict two of the remaining three measurements. Allowing η_{H_2O} to vary in the fitting of the individual profiles, we found that the best-fit values agreed to within 20% of the mean value (0.098) for the four measurements. We expect that this variability is caused primarily by laser fluctuations.
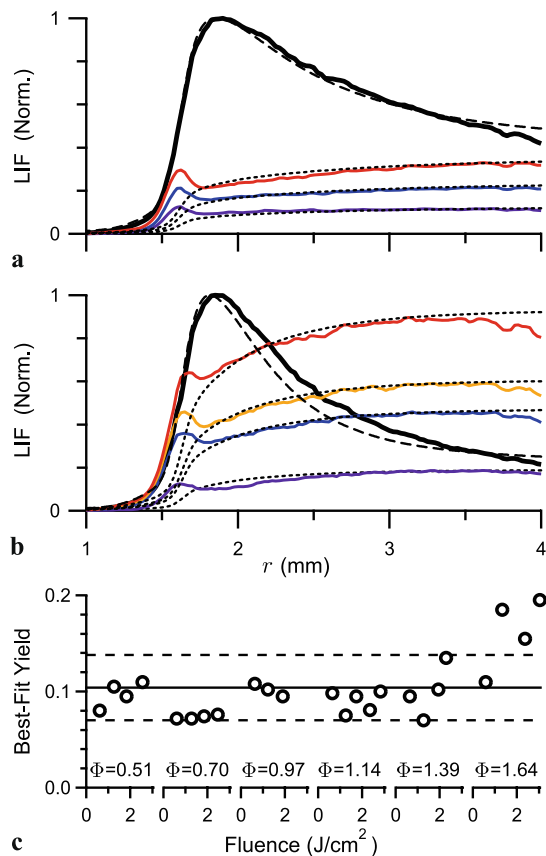
Fig. 7 Comparison of measured and simulated interference profiles using (1) and (2) with OH photodissociation and H_2O absorption cross sections from [16] and [29], respectively. (**a**) Fitted data from the $\Phi = 0.97$ flame (Fig. 6c) using $\eta_{H_2O} = 0.10$ for all three interference profiles; (**b**) Fitted data from the $\Phi = 0.51$ flame (Fig. 6a) using $\eta_{H_2O} = 0.08$, 0.105, 0.095, and 0.11 for profiles with pump fluence of 0.62, 1.26, 1.83, and 2.55 $J\,cm^{-2}$, respectively. Fitted profiles are shown as *dotted curves*, and the *dashed curves* are simulated LIF profiles for nascent H-atoms in each flame. (**c**) Summary of best-fit values of η_{H_2O} in the six flames. The mean is 0.104 (*solid line*) with a standard deviation of 0.035 (*dashed lines*)

A summary of the best-fit values for η_{H_2O} for all six flames is shown in Fig. 7c. The mean yield is 0.10, and the standard deviation is 0.035. In some cases (see, for example, the 0.65 $J\,cm^{-2}$ profile in Fig. 6d), we observed slight changes in the shape of the interference profiles at different pump energies and were not able to ascertain a best-fit for the detected yield. These profiles were excluded from the analysis. The observed changes in the profile shape may be attributed to pointing instabilities of the UV laser beams causing a change in the overlap of the beams. Overall, however, we observed excellent fits to the shape of the measured interference profiles and consistent fitted values of η_{H_2O}, suggesting that photodissociation of H_2O is the primary cause of interference in the product region of these flames. The same analysis using results of flame calculations employing the Miller Mechanism produced a mean yield of

6.5%, which provides an indication of the bounds on the estimated yield. The lower yield is a result of the lower peak H-atom number densities predicted by the Miller Mechanism.

The effective cross section for production of interfering H atoms is equal to the product of the absorption cross section and the fitted value for the yield. Using a mean yield of 0.1 and absorption cross sections based on the calculated temperature at $r = 2.6$ mm, we estimate that the effective H_2O cross section ranges from 0.8×10^{-20} cm^2 in the leanest flame to 1.2×10^{-20} cm^2 in the richest flame. This result is in excellent agreement with the previous report by Goldsmith [13], who inferred a photolysis cross section of 10^{-20} cm^2, based on the increase in OH LIF signal that was produced by a 205-nm photolysis laser in an atmospheric-pressure H_2/O_2 flame. The temperature in Goldsmith's experiment was only 1500 K, however, and the agreement between the current results and Goldsmith's cross section is surprising because the H_2O absorption cross section at 205 nm increases by an order of magnitude as temperature is increased from 1500 to 2800 K [29].

6.2 Interference in the flame front

The contribution to the interference from photodissociated H_2O and OH in the product region was subtracted from the measured interference signal to isolate the interference that was produced by intermediate species in the flame front. Figure 8 shows the interference profiles in the six flames that result from an analysis using GRI-Mech. The vertical scale in each plot is normalized to the peak TP-LIF signal from the nascent H atoms, and the pump pulse fluence is indicated in the legend.
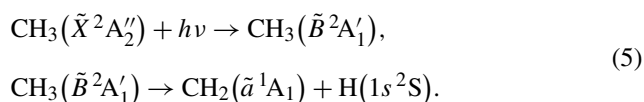
We consider the calculated radial distributions of the six most abundant H-containing intermediates in the six flames (Fig. 3). The six intermediates include methyl radical (CH_3), acetylene (C_2H_2), hydroperoxy radical (HO_2), formaldehyde (CH_2O), ethylene (C_2H_4), and ethane (C_2H_6). Unlike the case for H_2O in the product region, where $N_{H_2O} \gg N_H^{eq}$, the number densities of the potential intermediate precursors are on the order of or smaller than the peak number density of the nascent H atoms. To produce a large interference signal in the flame-front region, these precursors must have both a large absorption cross section, σ_i, at 205 nm and a large yield, η_i (see (2)).

Of these species, only methyl has been identified previously as a source of photolytic interference in flames [14, 15]. Acetylene, however, has been used as a photolytic precursor at 205 nm to produce H atoms in a discharge [17]. Photodissociation of CH_3 and C_2H_2 as well as photodissociation of the other four potential precursors shown in Fig. 3 are discussed in more detail below.

6.2.1 Methyl radical (CH$_3$)

The methyl radical has been identified as a relevant photolytic precursor producing atomic hydrogen in the reaction zone of methane flames [14, 15]. The origin band of the $\tilde{B}\,^2A'_1$–$\tilde{X}\,^2A''_2$ electronic system of CH$_3$ peaks near 216 nm [30], and the absorption spectrum extends below 204 nm into the dissociative continuum [31, 32]. In addition to the origin band, two broad vibronic features have been identified at shorter wavelengths. The (010-010) hot band is peaked near 212 nm [30, 32, 33], and a much broader feature that is peaked near 207 nm corresponds to the (100-000) band [32, 33]. The broad structure of the (100-000) band corresponds to a $\tilde{B}\,^2A'_1(v_1 = 1)$ lifetime of only 13 fs [33], which can be compared to the relatively longer predissociative lifetime of approximately 60 fs in the origin band [34, 35].
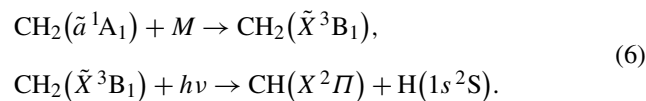
Following excitation to $\tilde{B}\,^2A'_1$, three energetically allowed dissociation pathways are possible [36]. Two of these pathways result in H + CH$_2$ products, and the third produces H$_2$ + CH. In an investigation of the photodissociation of CH$_3$ in the dissociative continuum at 193.3 nm, North et al. [31] demonstrated that the only dissociation products are CH$_2$ and H. Furthermore, the measured translational energy distributions strongly suggest that the methylene product was in the low-lying singlet state ($\tilde{a}\,^1A_1$) rather than in the ground state ($\tilde{X}\,^3B_1$), in accord with theory [36]. Wilson et al. [37] and Wu et al. [38] studied photodissociation at 216 and 212.6 nm, respectively. Both groups also concluded that the methylene photoproduct is formed in the singlet state, based on energetic considerations and measured translational energy spectra. Based on these results at 193, 212, and 216 nm, we assume that the dominant pathway for photodissociation of CH$_3$ at 205 nm is

$$CH_3\big(\tilde{X}\,^2A''_2\big) + h\nu \rightarrow CH_3\big(\tilde{B}\,^2A'_1\big),$$
$$CH_3\big(\tilde{B}\,^2A'_1\big) \rightarrow CH_2\big(\tilde{a}\,^1A_1\big) + H\big(1s\,^2S\big). \tag{5}$$

Although most measurements of the CH$_3$ UV absorption cross section focus on the origin band (see, for example, [39] and references therein), Callear and Metcalfe [32] and Glanzer et al. [40] report the UV absorption spectra between 204 and 218 nm. To our knowledge, the only high-temperature absorption cross-section measurement near 205 nm is published by Glanzer et al. [40], who report a value greater than 10^{-18} cm^2 at 205 nm for 1400 K. Based on the temperature dependence of the population in the electronic and vibrational ground state, we expect that the absorption cross section decreases only slightly between 1400 K and the peak temperatures in the current flames. The large absorption cross section at all relevant temperatures leads to saturation even at the lowest laser fluence of 0.6 J/cm^2.

We estimate the maximum interference that can result from single-photon dissociation of CH$_3$ as follows. The calculated methyl number density profile was convolved with the spatial response function, $g(r)$, and normalized by the peak number density of nascent H atoms to compare the observed interference profiles to the calculated profiles that would result if every CH$_3$ molecule dissociated and produced a detected H-atom. The resulting profiles using calculations with GRI-Mech 3.0 are shown as dotted curves in Fig. 8, demonstrating excellent spatial overlap with the measured interference near the flame front. The magnitudes of the calculated CH$_3$ profiles are comparable to the measured interferences at the highest fluences in most flames, but the simulation significantly underpredicts the observed interference in the $\Phi = 1.64$ flame. To explain the magnitude of the observed interference signals in Fig. 8 by single-photon photodissociation of CH$_3$, one must assume near-complete single-photon dissociation of this precursor at the highest fluences. Gasnot et al. [15] made a similar observation in a low-pressure methane flame. Here, especially in the case of the $\Phi = 1.64$ flame, we must infer that additional photolytic contributions are important as well. In the following sections, we discuss the other potential nascent precursors, but we also must consider the photodissociation of the singlet methylene that results from CH$_3$ dissociation.

Desgroux et al. [14] addressed the subsequent absorption of 205-nm photons in the sequential dissociation of CH$_3$ and its products to explain the observation of CH photofragment fluorescence in flames. Contrary to the explanation in [14], we expect that rapid collision-induced intersystem crossing (CIISC) is necessary to relax a fraction of the singlet methylene photoproduct to its triplet ground state, as opposed to a crossing in the CH$_3$ excited state that occurs prior to its dissociation [41–44]. If the CH$_2$ CIISC is sufficiently fast relative to the laser pulse duration, subsequent absorption from the triplet ground state to the first triplet excited state leads to a barrierless dissociation [18, 45, 46],

$$CH_2\big(\tilde{a}\,^1A_1\big) + M \rightarrow CH_2\big(\tilde{X}\,^3B_1\big),$$
$$CH_2\big(\tilde{X}\,^3B_1\big) + h\nu \rightarrow CH\big(X\,^2\Pi\big) + H\big(1s\,^2S\big). \tag{6}$$

Ab initio calculations predict a large transition dipole moment for the CH$_2$ absorption that peaks near 201 nm, and the calculated absorption cross section at 205 nm is approximately 5×10^{-18} cm^2 [47]. Thus, we expect that the photodissociation of CH$_2$ is strongly saturated at the pulse fluences used in the current experiments, and only CIISC limits the production of a second H atom from the CH$_3$ precursor.

Subsequent photodissociation of the CH fragment also generates a ground-state H atom. At 205 nm, the large transition moment coupling the ground state and the repulsive

Fig. 8 Relative photolytic-interference profiles resulting from transient intermediate species for a range of pump fluence in each of the six $CH_4/O_2/N_2$ flames with equivalence ratios: (**a**) 0.51, (**b**) 0.70, (**c**) 0.97, (**d**) 1.14, (**e**) 1.39, and (**f**) 1.64. Interference profiles are scaled relative to the nascent profile in each flame. Pump fluence [J cm^{-2}] is indicated in the legend. The measured interference profiles in Fig. 6 were corrected for the contribution from photodissociation of H_2O and OH. Convolutions (1) of N_{CH_3} and $N_{C_2H_2}$ are shown as the *dotted* and *dashed* curves, respectively
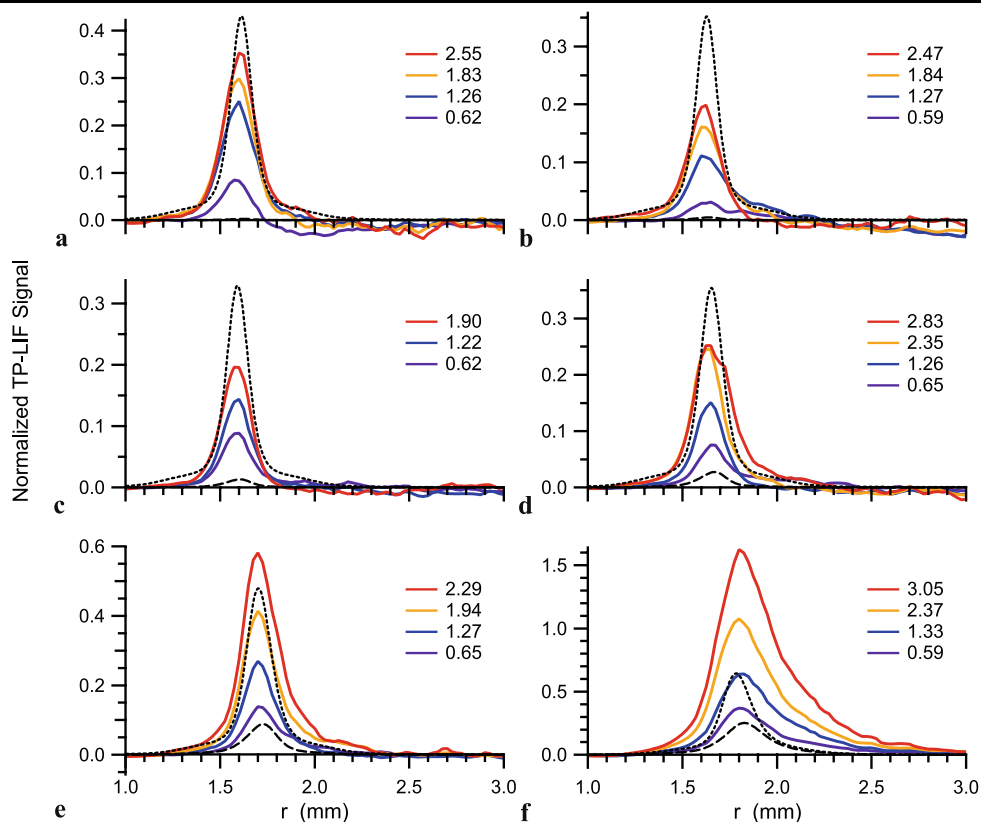
$2\,^2\Sigma^+$ state leads to effective photodissociation of the CH radical,

$$CH(X\,^2\Pi) + h\nu \rightarrow CH(2\,^2\Sigma^+),$$
$$CH(2\,^2\Sigma^+) \rightarrow C + H(1s\,^2S).$$
(7)
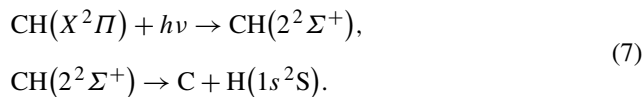
Although the $CH(2\,^2\Sigma^+)$ state correlates with the excited $C(^1S)$ state, interaction with the $CH(C\,^2\Sigma^+)$ state can also lead to the $C(^1D)$ product [48]. Regardless of the electronic state of the product carbon atom, the H atom is again produced in its ground state. The calculated absorption cross section for excitation at 205 nm is 2.5×10^{-18} cm^2 [48]. Therefore, this process is also expected to be saturated at the fluences used in the current experiments, and the production of three H atoms from the complete photodissociation of CH_3 by the sequential absorption of three 205-nm photons is feasible.

Figure 9 presents results of the same analysis that produced Fig. 8 excepts that the Miller Mechanism was used instead of GRI-Mech 3.0. Comparison of the computed CH_3 profiles with the measured interference profiles in Fig. 9 further supports the significant role of methyl as a precursor. The larger relative methyl number densities predicted by the Miller Mechanism for the lean and near stoichiometric flames suggest that the interferences could be produced by removal of a single hydrogen atom from CH_3 with less than unity quantum yield. In the two richest flames, this scenario

may also be plausible if the photodissociation of acetylene is included, as discussed next.
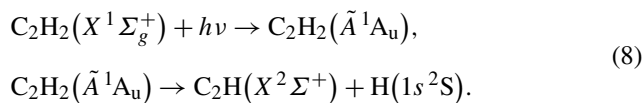
6.2.2 Acetylene (C_2H_2)

Acetylene is present in relatively high concentration only in the rich flames. In the $\Phi = 0.97$ flame, the ratio of the peak number density of C_2H_2 to that of atomic hydrogen in the GRI-Mech calculation is only 2%. This ratio is approximately 16% in the calculations using the Miller Mechanism. The ratio increases with increasing equivalence ratio. In the $\Phi = 1.64$ flame, it approaches 50% in the GRI-Mech calculation and exceeds 110% in the calculation using the Miller Mechanism. For comparison to the measured interference signals, the maximum interference that results from removal of an H atom from each C_2H_2 molecule was calculated by convolving the acetylene number density profile with the spatial response function and normalizing by the peak of H-atom number density. The results are shown as the dashed curves in Figs. 8 and 9 for analyses using GRI-Mech and the Miller Mechanism, respectively. The spatial distributions of the profiles for C_2H_2 overlap well with the measured interference profiles. The shape and peak locations of the CH_3 and C_2H_2 profiles are almost identical in all but the richest flame. In the $\Phi = 1.64$ flame, the C_2H_2 profile is slightly asymmetric and extends further into the products. Qualitatively, the same trend is observed in the measured

Fig. 9 Same as Fig. 8, but using the Miller Mechanism instead of GRI-Mech for the computed species and temperature used in the analysis
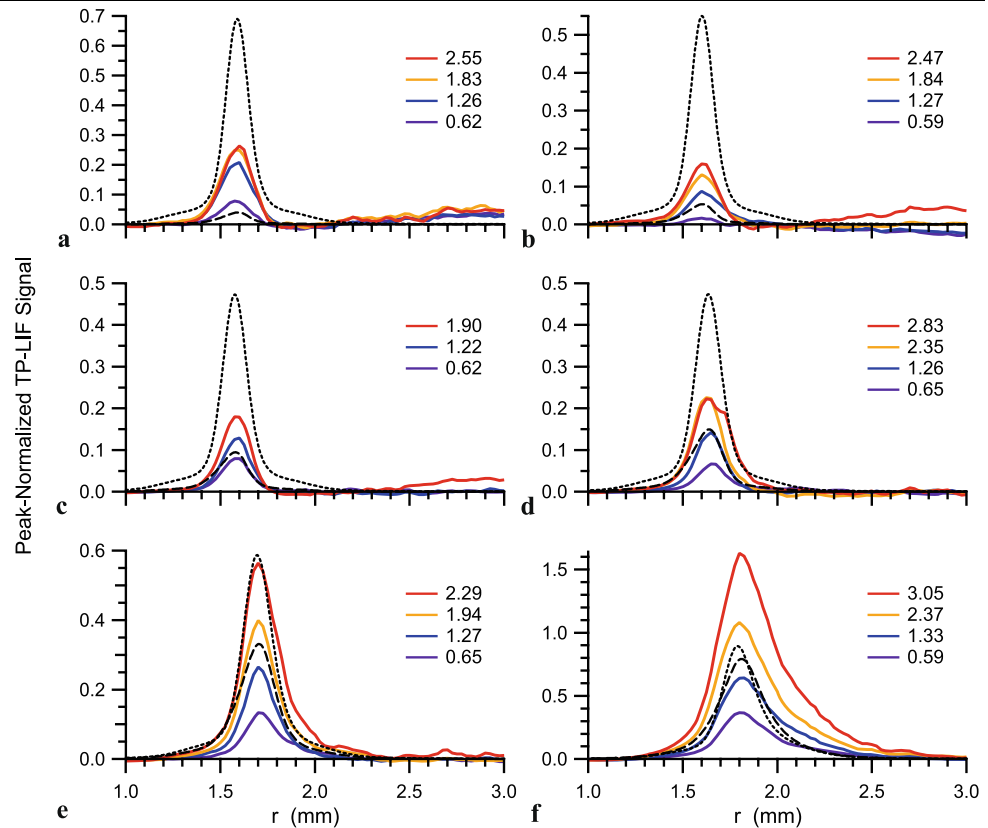
interference profiles in the richest flame in Figs. 8 and 9. The magnitude of the C_2H_2 contribution is less significant than that expected from CH_3, but the potential interference from C_2H_2 becomes increasingly important with increasing equivalence ratio, especially in calculations using Miller's Mechanism.

The $\tilde{A}\,^1A_u - X\,^1\Sigma_g^+$ system of acetylene is composed of a complex rovibronic structure that extends from 190–240 nm [49, 50]. The bond energy $D_0(H\text{-}CCH)$ for removal of an H atom corresponds to a 217-nm photon [51], and 205-nm excitation results in predissociation [52, 53]

$$C_2H_2\big(X\,^1\Sigma_g^+\big) + h\nu \rightarrow C_2H_2\big(\tilde{A}\,^1A_u\big),$$

$$C_2H_2\big(\tilde{A}\,^1A_u\big) \rightarrow C_2H\big(X\,^2\Sigma^+\big) + H\big(1s\,^2S\big). \tag{8}$$

Although earlier studies suggested a relatively low quantum yield for the C–H bond fission channel in Reaction 8 [54, 55], more recent results indicate that the dissociation is the primary channel with close to unity yield [52, 56].

The reported room-temperature absorption cross section for C_2H_2 at 205 nm is approximately 2×10^{-20} cm^2 [57], but a strong temperature dependence is expected as a result of contributions from vibrationally excited C_2H_2. Vattulainen et al. [58] measured a strong increase in the absorption cross section between room temperature and 1073 K, at which the cross section increases to 4×10^{-19} cm^2. In

accord with the results in [58], Franck–Condon calculations also indicate approximately a factor of 15–20 increase in the absorption cross section between room temperature and 1073 K [59]. At higher temperatures, however, the calculated cross section decreases, and we estimate a value of approximately 10^{-19} cm^2 at flame temperatures. Therefore, at the highest fluences used in the current experiments, slight saturation of Reaction 8 is expected, dissociating approximately 30% of the C_2H_2 molecules.

Subsequent photodissociation of the ethynyl product produces a second H atom from the C_2H_2 precursor molecule [53, 60–63],

$$C_2H\big(X\,^2\Sigma^+\big) + h\nu \rightarrow C_2 + H\big(1s\,^2S\big), \tag{9}$$
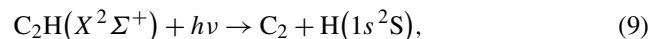
where the C_2 product state depends critically on the vibrational state of the ethynyl radical [62].

Although acetylene can have little impact on the interference in the lean flames, the number density of C_2H_2 increases dramatically with increasing equivalence ratio. The peak C_2H_2 number density is comparable to the H-atom number density at $r = 2$ mm location in the richest flame. Although it appears that C_2H_2 photodissociation has a smaller effect than CH_3 in the current flames, we expect that this process will be particularly important in flames of higher molecular weight fuels, where C_2 species densities are much larger.

6.2.3 Hydroperoxy radical (HO$_2$)

The peak hydroperoxy radical number density is approximately 25% that of atomic hydrogen in the $\Phi = 0.51$ flame, and its relative significance decreases with increasing equivalence ratio. The UV absorption cross section of HO$_2$ peaks near 205 nm and is very broad, suggesting rapid dissociation. The UV absorption has been measured by several groups. Tyndall et al. [64] review the measurements and recommend a room-temperature absorption cross section of 4.65×10^{-18} cm^2. Although the large absorption cross section and relatively high concentration in the lean flames might implicate HO$_2$ as a relevant H-atom precursor, electronic structure calculations indicate that barriers of repulsive excited states along the O–H stretching coordinate prevent formation of O$_2$ + H products for photon energies below 6.5 eV ($\lambda > 191$ nm) [65, 66]. Therefore, we can assume that $\eta_{HO_2} = 0$, and eliminate HO$_2$ from the list of potential precursors.

6.2.4 Formaldehyde (CH$_2$O)

In all six flames, the calculated peak CH$_2$O number density is approximately 10^{16} cm^{-3}, which is 20–50% of the peak H-atom number density. Figure 3 shows that the formaldehyde number density peaks closer to the reactants than methyl. Although ultraviolet photodissociation of CH$_2$O can produce atomic hydrogen [67, 68], excitation at 205 nm lies between the ultraviolet $\tilde{A}\,^1A_2 - \tilde{X}\,^1A_1$ system and VUV Rydberg transitions [69]. The UV absorption cross section falls off with decreasing wavelength from its peak value near 300 nm, and the absorption cross section is less than 3×10^{-22} cm^2 at 226 nm [70]. In the VUV, absorption is only significant at wavelengths shorter than 180 nm [69, 71]. Thus, despite its appreciable concentration in the flames, we expect that photodissociation of formaldehyde has a negligible effect on the H-atom concentration.

6.2.5 Ethylene (C$_2$H$_4$)

Although the concentration of ethylene is significant and photolytic production of H atoms is energetically possible at 205 nm [72], we do not expect any measurable interference from this species. The absorption bands of C$_2$H$_4$ lie in the VUV and are most significant at wavelengths shorter than 180 nm [73]. Orkin et al. [74] report a cross section of only 10^{-22} cm^2 at 205 nm. Thus, the estimated production of H atoms from C$_2$H$_4$ is negligible even at the highest fluences used in the current experiments.

6.2.6 Ethane (C$_2$H$_6$)

Like the other two C$_2$ species considered here, the ethane number density becomes increasingly significant in rich flames, and if relevant, the sequential removal of multiple H atoms from each precursor molecule could result in a major interference for detection of H atoms. But as with C$_2$H$_4$, removal of the first H atom from C$_2$H$_6$ is improbable at 205 nm. The absorption cross section of C$_2$H$_6$, like that of all straight-chain alkanes, is peaked at wavelengths shorter than 100 nm and falls off to values less than 10^{-22} cm^2 for wavelengths longer than approximately 160 nm [75]. Equation (2) predicts that such a weak absorber cannot contribute significantly to the observed photolytic interference in the current experiments. At the highest fluence used in the current experiments, for an absorption cross section of 10^{-22} cm^2, $N_{\mathrm{H}}^{\mathrm{ph}}/N_{\mathrm{C_2H_6}}^{\mathrm{eq}}$ is less than 3×10^{-4}.

7 Conclusions

A pump-probe technique was used to measure spatial distributions of hydrogen atoms that are photolytically produced in premixed methane flames. Results of 1-D flame calculations using well known mechanisms were used in conjunction with the measurements to identify the potential photolytic precursor molecules. Photophysical properties of the suspect molecules were considered.

The spatial distributions of photolytically produced H atoms clearly indicate contributions from intermediate and product species in the flames. In accord with earlier investigations, we infer a significant contribution to the measured interference from vibrationally excited H$_2$O in the product region. Additionally, for the first time, we suggest that photodissociation of vibrationally excited OH may also contribute to the interference. Using published temperature-dependent absorption cross sections for H$_2$O and OH, we demonstrate excellent agreement between simulated and measured interference profiles in all flames.

The spatially resolved measurements indicate an important interference occurs in the flame-front region, very near to the location of peak H-atom number density. Interference from intermediate species is evident even in the leanest flame ($\Phi = 0.5$) and becomes increasingly significant as the equivalence ratio increases. In the richest flame ($\Phi = 1.6$), the dominant interference occurs in the flame-front region and is 60% larger than the signal from nascent H atoms at the highest laser fluence used (3 J cm^{-2}). As reported previously, the most significant intermediate precursor is CH$_3$, but here we also argue that C$_2$H$_2$ photodissociation can contribute to the interference, and may be especially important in flames using heavier fuels. The increasing significance of C$_2$H$_2$ photodissociation in rich flames is underscored in the results of the 1-D flame calculations using the Miller Mechanism, which predicts comparable number densities of CH$_3$ and C$_2$H$_2$ in the richest flame investigated here. We present the mechanisms for the sequential photodissociation

of CH_3 and C_2H_2. The mechanisms indicate complete dissociation of each species is feasible, and saturation of the single-photon absorption steps is probable for the fluences used in the current study. Additionally, by considering the published photophysical properties of HO_2, CH_2O, C_2H_4, and C_2H_6, we exclude these species as potentially significant precursors despite their large concentrations in the current flames.

References

1. R.P. Lucht, J.T. Salmon, G.B. King, D.W. Sweeney, N.M. Laurendeau, Opt. Lett. **8**, 365 (1983)
2. J.T. Salmon, N.M. Laurendeau, Appl. Opt. **26**, 2881 (1987)
3. J.T. Salmon, N.M. Laurendeau, Combust. Flame **74**, 221 (1988)
4. J.E.M. Goldsmith, Proc. Combust. Inst. **22**, 1403 (1988)
5. M. Aldén, A.L. Schawlow, S. Svanberg, W. Wendt, P.L. Zhang, Opt. Lett. **9**, 211 (1984)
6. K.E. Bertagnolli, R.P. Lucht, M.N. Bui-Pham, J. Appl. Phys. **83**, 2315 (1998)
7. A. Brockhinke, A. Bülter, J.C. Rolon, K. Kohse-Höinghaus, Appl. Phys. B **72**, 491 (2001)
8. J.E.M. Goldsmith, Opt. Lett. **10**, 116 (1985)
9. S.J. Harris, A.M. Weiner, R.J. Blint, J.E.M. Goldsmith, Proc. Combust. Inst. **21**, 1033 (1986)
10. J.E.M. Goldsmith, N.M. Laurendeau, Opt. Lett. **15**, 576 (1990)
11. N. Georgiev, M. Aldén, Appl. Spectrosc. **51**, 1229 (1997)
12. W.D. Kulatilaka, J.H. Frank, T.B. Settersten, Proc. Combust. Inst. **32**, 955 (2009)
13. J.E.M. Goldsmith, Opt. Lett. **11**, 416 (1986)
14. P. Desgroux, L. Gasnot, B. Crunelle, J.F. Pauwels, Proc. Combust. Inst. **26**, 967 (1996)
15. L. Gasnot, P. Desgroux, J.F. Pauwels, L.R. Sochet, Appl. Phys. B **65**, 639 (1997)
16. D.Č. Radenović, A.J.A. van Roij, S.-M. Wu, J.J. ter Meulen, D.H. Parker, M.P.J. van der Loo, L.M.C. Janssen, G.C. Groenenboom, Mol. Phys. **106**, 557 (2008)
17. B.L. Preppernau, K. Pearce, A. Tserepi, E. Wurzberg, T.A. Miller, Chem. Phys. **196**, 371 (1995)
18. G. Baravian, G. Sultan, J. Amorim, C. Hayaud, J. Appl. Phys. **82**, 3615 (1997)
19. R. Quandt, X.B. Wang, Z.Y. Min, H.L. Kim, R. Bersohn, J. Phys. Chem. A **102**, 6063 (1998)
20. W.D. Kulatilaka, B.D. Patterson, J.H. Frank, T.B. Settersten, Appl. Opt. **47**, 4672 (2008)
21. J.H. Frank, X. Chen, B.D. Patterson, T.B. Settersten, Appl. Opt. **43**, 2588 (2004)
22. P.P. Yaney, D.A.V. Kliner, P.E. Schrader, R.L. Farrow, Rev. Sci. Inst. **71**, 1296 (2000)
23. R.J. Kee, J. Grcar, M.D. Smooke, J.A. Miller, *A Fortran program for modeling steady laminar one-dimensional premixed flames*. Tech. Rep. SAND85-8240, Sandia National Laboratories (1985)
24. G.P. Smith, D.M. Golden, M. Frenklach, N.W. Moriarty, B. Eiteneer, M. Goldenberg, C.T. Bowman, R.K. Hanson, S. Song, W.C. Gardiner Jr., V.V. Lissianski, Z. Qin, available from: http://www.me.berkeley.edu/gri_mech/ (2000)
25. N. Hansen, J.A. Miller, T. Kasper, K. Kohse-Höinghaus, P.R. Westmoreland, J. Wang, T.A. Cool, Proc. Combust. Inst. **32**, 623 (2009)
26. G.H. Dieke, Phys. Rev. **50**, 797 (1936)
27. G. Herzberg, L.L. Howe, Can. J. Phys. **37**, 636 (1959)
28. V. Engel, V. Staemmler, R.L. Vander Wal, F.F. Crim, R.J. Sension, B. Hudson, P. Andresen, S. Hennig, K. Weide, R. Schinke, J. Phys. Chem. **96**, 3201 (1992)
29. C. Schulz, J.B. Jeffries, D.F. Davidson, J.D. Koch, J. Wolfrum, R.K. Hanson, Proc. Combust. Inst. **29**, 2735 (2002)
30. G. Herzberg, Proc. R. Soc. Lond., Ser. A **262**, 291 (1961)
31. S.W. North, D.A. Blank, P.M. Chu, Y.T. Lee, J. Chem. Phys. **102**, 792 (1995)
32. A.B. Callear, M.P. Metcalfe, Chem. Phys. **14**, 275 (1976)
33. S.G. Westre, T.E. Gansberg, P.B. Kelly, L.D. Ziegler, J. Phys. Chem. **96**, 3610 (1992)
34. S.G. Westre, P.B. Kelly, Y.P. Zhang, L.D. Ziegler, J. Chem. Phys. **94**, 270 (1991)
35. T.B. Settersten, R.L. Farrow, J.A. Gray, Chem. Phys. Lett. **370**, 204 (2003)
36. H.T. Yu, A. Sevin, E. Kassab, E.M. Evleth, J. Chem. Phys. **80**, 2049 (1984)
37. S.H.S. Wilson, J.D. Howe, K.N. Rosser, M.N.R. Ashfold, R.N. Dixon, Chem. Phys. Lett. **227**, 456 (1994)
38. G. Wu, B. Jiang, Q. Ran, J. Zhang, S.A. Harich, X. Yang, J. Chem. Phys. **120**, 2193 (2004)
39. M.A. Oehlschlaeger, D.F. Davidson, R.K. Hanson, J. Quant. Spectrosc. Radiat. Transfer **92**, 393 (2005)
40. K. Glänzer, M. Quack, J. Troe, Proc. Combust. Inst. **16**, 949 (1977)
41. U. Bley, F. Temps, J. Chem. Phys. **98**, 1058 (1993)
42. F. Hayes, W.D. Lawrance, W.S. Staker, K.D. King, J. Phys. Chem. **100**, 11314 (1996)
43. M.A. Blitz, K.W. McKee, M.J. Pilling, P.W. Seakins, Chem. Phys. Lett. **372**, 295 (2003)
44. A.V. Komissarov, A. Lin, T.J. Sears, G.E. Hall, J. Chem. Phys. **125**, 084308 (2006)
45. R.A. Beärda, M.C. van Hemert, E.F. van Dishoeck, J. Chem. Phys. **97**, 8240 (1992)
46. B. Bohn, F. Stuhl, J. Chem. Phys. **102**, 8842 (1995)
47. G.-J. Kroes, E.F. van Dishoeck, R.A. Beärda, M.C. van Hemert, J. Chem. Phys. **99**, 228 (1993)
48. E.F. van Dishoeck, J. Chem. Phys. **86**, 196 (1987)
49. C.K. Ingold, G.W. King, J. Chem. Soc. 2725–2744 (1953)
50. K.K. Innes, J. Chem. Phys. **22**, 863 (1954)
51. D.H. Mordaunt, M.N.R. Ashfold, J. Chem. Phys. **101**, 2630 (1994)
52. D.H. Mordaunt, M.N.R. Ashfold, R.N. Dixon, P. Löffler, L. Schnieder, K.H. Welge, J. Chem. Phys. **108**, 519 (1998)
53. D.P. Baldwin, M.A. Buntine, D.W. Chandler, J. Chem. Phys. **93**, 6578 (1990)
54. S. Satyapal, R. Bersohn, J. Phys. Chem. **95**, 8004 (1991)
55. K. Seki, H. Okabe, J. Phys. Chem. **97**, 5284 (1993)
56. N. Hashimoto, N. Yonekura, T. Suzuki, Chem. Phys. Lett. **264**, 545 (1997)
57. F.Z. Chen, D.L. Judge, C.Y.R. Wu, J. Caldwell, H.P. White, R. Wagener, J. Geophys. Res. **96**, 17519 (1991)
58. J. Vattulainen, L. Wallenius, J. Stenberg, R. Hernberg, V. Linna, Appl. Spectrosc. **51**, 1311 (1997)

59. D.L. Osborn, private communication (2008)
60. A.M. Wodtke, Y.T. Lee, J. Phys. Chem. **89**, 4744 (1985)
61. B.A. Balko, J. Zhang, Y.T. Lee, J. Chem. Phys. **94**, 7958 (1991)
62. A.M. Mebel, M. Hayashi, W.M. Jackson, J. Wrobel, M. Green, D. Xu, S.H. Lin, J. Chem. Phys. **114**, 9821 (2001)
63. A. Läuter, K.S. Lee, K.H. Jung, R.K. Vatsa, J.P. Mittal, H.-R. Volpp, Chem. Phys. Lett. **358**, 314 (2002)
64. G.S. Tyndall, R.A. Cox, C. Granier, R. Lesclaux, G.K. Moortgat, M.J. Pilling, A.R. Ravishankara, T.J. Wallington, J. Geophys. Res. **106**, 12157 (2001)
65. S.R. Langhoff, R.L. Jaffe, J. Chem. Phys. **71**, 1475 (1979)
66. G.J. Vazquez, S.D. Peyerimhoff, R.J. Buenker, Chem. Phys. **99**, 239 (1985)
67. B.A. DeGraff, J.G. Calvert, J. Am. Chem. Soc. **89**, 2247 (1967)
68. R.D. McQuigg, J.G. Calvert, J. Am. Chem. Soc. **91**, 1590 (1969)
69. D.C. Moule, A.D. Walsh, Chem. Rev. **75**, 67 (1975)
70. R. Meller, G.K. Moortgat, J. Geophys. Res. **105**, 7089 (2000)
71. G. Cooper, J.E. Anderson, C.E. Brion, Chem. Phys. **209**, 61 (1996)
72. H. Shiromaru, Y. Achiba, K. Kimura, Y.T. Lee, J. Phys. Chem. **91**, 17 (1987)
73. M.E. Zelikoff, K. Watanabe, J. Opt. Soc. Am. **43**, 756 (1953)
74. V.L. Orkin, R.E. Huie, M.J. Kurylo, J. Phys. Chem. **101**, 9118 (1997)
75. A.Y.T. Lee, Y.L. Yung, B.-M. Cheng, M. Bahou, C.-Y. Chung, Y.-P. Lee, Astrophys. J. **551**, L93 (2001)